Surface of glassy GeS[subscript 2]: A model based on a first-principles approach

Surface of glassy GeS_2: A model based on a first-principles approach

G. Ori,[1,2] C. Massobrio,[3] A. Bouzid,[3] M. Boero,[3] and B. Coasne[1,2,4,*]

[1]*Institut Charles Gerhard Montpellier, CNRS (UMR 5253), ENSCM, Universite Montpellier 2, 8 rue de l'Ecole Normale, 34296 Montpellier Cedex 5, France*

[2]*Multiscale Material Science for Energy and Environment ⟨MSE⟩[2], UMI 3466 CNRS-MIT, 77 Massachusetts Avenue, Cambridge, Massachusetts, USA*

[3]*Institut de Physique et Chimie des Matériaux de Strasbourg CNRS-UMR 7504,23 rue du Loess 67034 Strasbourg Cedex 2, France*

[4]*Department of Civil and Environmental Engineering, Massachusetts Institute of Technology, Massachusetts, USA*

(Received 6 October 2013; revised manuscript received 6 July 2014; published 25 July 2014)

First-principles calculations within the framework of the density functional theory are used to construct realistic models for the surface of glassy GeS_2 (g-GeS_2). Both calculations at $T = 0$ K and at finite temperature ($T = 300$ K) are considered. This allows for a comparison between the structural and electronic properties of surface and bulk g-GeS_2. Although the g-GeS_2 surface recovers the main tetrahedral structural motif of bulk g-GeS_2, the number of fourfold coordinated Ge atoms and twofold coordinated S atoms is smaller than in the bulk. On the contrary, the surface system features a larger content of overcoordinated S atoms and threefold coordinated Ge atoms. This effect is more important for the g-GeS_2 surface relaxed at 0 K. Maximally localized Wannier functions (WF) are used to inspect the nature of the chemical bonds of the structural units present at the g-GeS_2 surface. We compare the ability of several charge derivation methods to capture the atomic charge variations induced by a coordination change. Our estimate for the charges allows exploiting the first-principles results as a data base to construct a reliable interatomic force field.

DOI: 10.1103/PhysRevB.90.045423 PACS number(s): 61.43.Fs, 68.35.bj, 77.84.Bw, 71.15.Pd

I. INTRODUCTION

Amorphous chalcogenides are defined as made up of chalcogen elements (S, Se, and/or Te) possessing a glassy architecture at the molecular level [1–3]. As a subclass of these materials, chalcogenide glassy films are useful for many applications such as optoelectronic and nonvolatile memory devices [4,5]. For example, amorphous $Ge_2Sb_2Te_5$ and GeS_x films prepared by deposition techniques can be used as phase-change and optical materials, respectively [6,7]. The structure and chemical order of these films are found to be strongly dependent on the chalcogenide composition and conditions used for the deposition. In some cases, these structures largely differ (in terms of quantity of defects) from those obtained by the common melt-quenching (MQ) technique used for the preparation of bulk glasses. It appears that g-GeS_x (with $x = 2, 4, 6$) films, obtained by pulsed laser deposition from the pristine bulk glasses (obtained by MQ), show a significant content of defects and "wrong bonds" [7–9]. In this case, the departure from perfect chemical order is due to the fact that as-deposited g-GeS_x films are far away from the equilibrium state [7]. For the case of glassy GeS_2 (g-GeS_2, g standing hereafter for glass), we recall that perfect chemical order corresponds to the absence of any undercoordinated or overcoordinated Ge atoms or S atoms ($\neq 4$ and $\neq 2$ for Ge and S, respectively).

As an alternative prototype of disordered systems strongly dependent on surface properties, investigations have also focused on the synthesis and characterization of nanochalcogenides such as nanoporous chalcogenide glasses (also referred to as chalcogels) [10–13]. In this case, common synthesis methods are based on nucleation-to-growth or linker-driven assembly of building units where the final structures can reach a state close to equilibrium. Obtaining in a controlled way such materials, which exhibit a large surface area from $\sim$10 to 500 m^2/g made up of highly polarizable atoms, can lead to breakthroughs for applications relying on the surface properties of the host compound (photocatalysis and gas separation, for instance) [14–16]. Recently, chalcogels have been demonstrated to be efficient sorbents for environmental remediation from gaseous and water waste media [17,18].

The specific motivation of this paper is to produce a glassy surface model capable of mimicking realistically the behavior of a chalcogel and its interfaces. The question arises on the atomic-scale structure of such compounds and on the analogies and differences with the bulk counterpart. When devising a model for such systems, the choice of a disordered slab obtained from the bulk structure is the most appropriate, since its final microscopic arrangement is independent on the kinetic effects characterizing a deposition process. Nonetheless, modeling an amorphous surface still represents a challenge, particularly because of the difficulties in cleaving from the bulk a proper plane in the absence of any reference as provided, for instance, by the Miller indices in the case of crystals. Yet, the practical realization of films or pores implies large exposed areas that simulations should be able to reproduce.

Given these premises, we report on the development of realistic atomic models of the g-GeS_2 surface by means of first-principles molecular dynamics (FPMD) based on fully self-consistent density functional theory. This approach has been well assessed and successfully employed to model bulk liquid and glassy chalcogenides [19–26]. Very recently, we were able to produce a bulk model for g-GeS_2 that featured an unprecedented agreement with neutron scattering data, thereby legitimating its further application to surface studies [27]. This bulk model was obtained by simulated melt quenching.

*coasne@mit.edu

Looking at previous available atomic-scale modeling in this domain, amorphous $GeSe_2$ surfaces were considered by the team of Drabold [28,29]. Chalcogenide surfaces were found to be characterized by a slight atomic expansion and a number of ring structures larger than in the bulk. One of the main features of bulk chalcogenide properties was also recovered, namely, the intermediate range order (IRO) through the appearance of the first sharp diffraction peak (FSDP) in the total neutron structure factor. Akola *et al.* [30] studied a computer-aided deposition (AD) of $Ge_2Sb_2Te_5$ by first-principles molecular dynamics. In comparison to the MQ structure, the AD model showed a different local environment for the Ge atoms (tetrahedral rather than the typical distorted octahedral found for this system) and the presence of "wrong bonds" (homopolar and Ge-Sb bonds). The structure factor and electronic properties of the two models were found to be very similar.

The present paper is organized as follows. Our theoretical model and computational framework is described in Sec. III A detailed account of the structure of the g-GeS_2 surface model is given in terms of pair correlation functions, structure factors, coordination numbers, and bond angle distributions (see Sec. III). Special attention is then devoted to the nature of chemical bonding as well as to the electronic and charge properties of the g-GeS_2 surface. In particular, the chemical bonding is analyzed by means of maximally localized Wannier functions (Sec. IV). With the aim of constructing an interatomic potential based on first-principles data, we also focus on the derivation of atomic charges for S and Ge atoms as obtained from various techniques. The availability of the model developed in this work is a necessary prerequisite to construct simplified, yet accurate, schemes for the study of chalcogenide glasses at the interface with other systems. Our conclusions are summarized in Sec. V.

II. THEORETICAL AND COMPUTATIONAL FRAMEWORK

A. First-principles molecular dynamics calculations

We adopted the method by Car and Parrinello [31] to ensure a self-consistent evolution of the electronic structure during molecular dynamics motion. The electronic structure was described in the framework of density functional theory (DFT) with the generalized gradient approximation (GGA) due to Becke (B) for the exchange energy and Lee, Yang, and Parr (LYP) for the correlation energy [32–34]. For the case of chalcogenides, we refer to Ref. [35] for a detailed account of the reasons underlying the better performances of the BLYP approach when compared, for instance, to the Perdew and Wang scheme. Here, we just recall that the BLYP exchange-correlation functional provides a better description of valence electron localization effects, which are crucial in the case of iono-covalent systems. Since van der Waals (vdW) interactions are found to be significant in some cases, for the present study, the BLYP functional was combined with the dispersion correction proposed by Grimme [36]. Such a correction is a thorough DFT-based empirical correction self-consistently tuned on different functionals, from PBE to B3LYP, and bechmarked on a wealth of different systems ranging from simple molecules to complex reactive surfaces [37–40]. No experimental parameter is included in the construction of this vdW correction and its inclusion does not affect at any stage the Kohn-Sham equations, thus preserving the first-principles character of the electronic structure calculations.

In our work, the valence electrons were treated explicitly, in conjunction with norm conserving pseudopotentials of the Trouiller-Martins [41] type to account for core-valence interactions. The wave functions were expanded at the γ point of the supercell on a plane-wave basis set with an energy cutoff $E_c = 20$ Ry. This energy cutoff value has already been shown to be fully adequate to attain converged properties for the relevant physical quantities of the Ge-S dimer (cohesive energy, interatomic distance, vibrational frequency). A fictitious electron mass of 1200 a.u. and a time step of $\Delta t = 0.1207$ fs are adopted to integrate the equations of motion. Simulations are performed for a fixed volume (NVT ensemble) for each step of sample generation and data collection. We start from a bulk sample of g-GeS_2 which was obtained in our previous work by using the same theoretical framework [27]. Such structural model can be safely considered as the best available for g-GeS_2, in spite of the fact that some peak intensities and features in both the total pair correlation function and the total neutron structure factor moderately differ from the experimental patterns.

In particular, we use the bulk model produced by the procedure labeled FPMD(1) in Ref. [27]. This model, which was equilibrated at 300 K, is labeled as g-$GeS_2(b)$ in what follows (b standing hereafter for bulk). The g-$GeS_2(b)$ sample is made up of 480 atoms, and has a volume of $23.576 \times 23.576 \times 23.576$ Å^3. As shown in Fig. 1, a g-GeS_2 surface was created by adding at the top and bottom of the g-$GeS_2(b)$ glass (along the z direction) empty volumes of a height 12 Å. In so doing, one obtains a g-GeS_2 slab exhibiting two surfaces embedded in a simulation box of a volume $23.576 \times 23.576 \times 47.576$ Å^3. Energy optimization

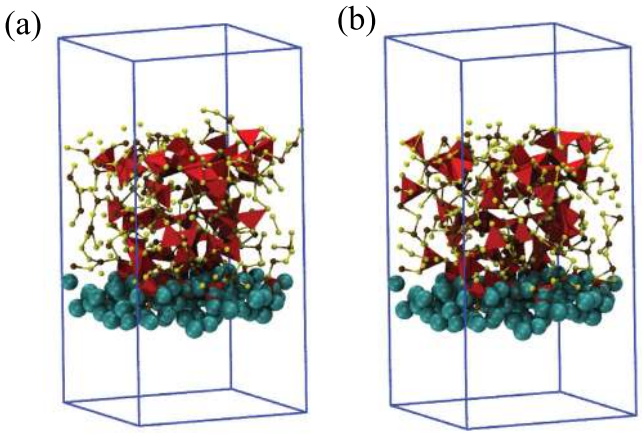

FIG. 1. (Color online) Typical molecular configuration of the 480 atoms forming the g-GeS_2 surface models refined at (a) 300 K [g-$GeS_2(s)$] and (b) 0 K [g-$GeS_2(s)$@0K]. For each system, the blue lines show the simulation box. Colors: S atoms in yellow and Ge atoms in ochre. Red tetrahedra show tetrahedrally coordinated Ge atoms. Cyan spheres are the bottom atoms kept frozen during the simulations (104 atoms).

via a steepest descent algorithm was employed to bring the material to $T = 0$ K and allow a first relaxation of all of the atoms. Then, we perform a FPMD run with a friction force (ion velocities scaled by a factor 0.95 at each step) for a total of 8500 steps so as to optimize the surface model at $T = 0$ K.

To produce a surface model at finite temperature, we employed the following layout. Keeping frozen the atoms within 5 Å from the bottom surface (104 atoms), the system was relaxed for 5 ps of microcanonical FPMD simulation (i.e., constant energy and volume). At the end of this run, the system reaches a constant temperature of about 140 K. The system was then gradually heated to 300 K during 2 ps by increasing the temperature in a stepwise manner with temperature intervals of 50 K. Temperature control was implemented for both ionic and electronic degrees of freedom using Nosé-Hoover thermostats [42–45]. The system was then equilibrated at 300 K for 20 ps and the last 15 ps were used for data collection. This surface is labeled hereafter as g-$GeS_2(s)$, where s stands for surface [Fig. 1(a)].

A second surface model was obtained by cooling down the model g-$GeS_2(s)$ to 0 K during 6 ps in a stepwise manner with intervals of 50 K ($q = 5 \times 10^{13}$ K/s). This model is labeled as g-$GeS_2(s)$@0K in what follows. Averages taken over three different starting surface configurations at 300 K are used to analyze the properties of g-$GeS_2(s)$@0K [Fig. 1(b)]. The three starting configurations were sampled every 6.67 ps, along the 20 ps FPMD simulation performed at 300 K, in order to ensure uncorrelated starting configurations. The g-$GeS_2(s)$@0K surface sample is found 0.24 eV/atom *more stable* with respect to the g-GeS_2 surface refined at 0 K without equilibration at room temperature. This shows that the surface bond rearrangements promoted by the equilibration at 300 K promote a further local stabilization with respect to mere optimization without annealing. However, this further local stabilization does not alter the S:Ge ratio as a function of the slab height, which remains close to stoichiometry (∼2).

B. Wannier functions

In order to probe the chemical bonding in the g-GeS_2 surface, we determined its electronic structure through the position of the maximally localized Wannier function centers [46–49]. The nth Wannier function $w_n(r)$ and the location of its center (x_n, y_n, z_n) are obtained as the unitary transformation of the Kohn-Sham orbitals $\psi_i(r)$ expressed as Bloch functions:

$$w_n(r) = \sum_i \left[\prod_p e^{-A^p_{i,n}} \psi_i(r) \right], \tag{1}$$

where $A^p_{i,n}$ is a matrix generalization of the Berry phase connector, p is the order of the iteration and i the wave vector [47]. The localization of the Wannier centers is determined by minimizing the spread functional Ω. This quantity is the difference between the Wannier charge density with respect to its own center of charge, thereby representing the spatial extension of the Wannier orbital:

$$\Omega = \sum_i (\langle i|r^2|i\rangle - \langle i|r|i\rangle^2). \tag{2}$$

The center of each Wannier orbital n is given by

$$x_n = -\frac{L_x}{2\pi} \mathrm{Im} \ln \langle w_n | e^{-\frac{i2\pi x}{L_x}} | w_n \rangle, \tag{3}$$

where L_x corresponds to the length of the simulation cell along x.

Similar equations are used for the coordinates along y and z. The center of the Wannier orbital indicates the maximum probability for the *location of an electron* (or *electron pair*) in a quantum system [47,48]. The analysis of the WF centers with respect to the nuclear positions allows gaining insight into the chemical bonding involved in systems such as water [50–52], amorphous silicon [53], and oxides [54]. This analysis has been extended to germanium selenides g-Ge_2Se_3, g-$GeSe_2$, g-$GeSe_3$, g-$GeSe_4$, and g-$GeSe_9$ where a complex mixture of ionocovalent and purely covalent bonds was found [20,26].

C. Charge calculation

Several methods have been developed to estimate atomic partial charges in polyatomic systems and provide useful insights into the nature of chemical bonding. These partial charges are often used in classical force fields. In this work, several charge-derivation techniques were used to estimate the atomic partial charges in the g-GeS_2 surface. The objective of this comparison is to determine the best suited method to describe the spatial distribution of the charges in the context of an empirical force-field. The following classical and first-principles-based methods were used.

(a) The *Qeq and EQeq methods* were derived from the original charge equilibration method developed by Rappe *et al.* [55,56]. In the Qeq method [55], the atomic charges are derived by considering that, at equilibrium, the electronic chemical potential is equal for all the atoms (A, B, etc.) in the system:

$$\chi_A(Q_1..Q_N) = \chi^0_A + Q_A J^0_{AA} + \sum_{A \neq B} Q_B J_{AB}, \tag{4}$$

where the electronegativity $\chi^0_A = (\frac{\partial E}{\partial Q})$ is the first derivative of the energy with respect to the charge. The latter quantity is an intrinsic property of chemical elements. J^0_{AA} and J_{AB} are the Coulomb repulsion between two electrons in the orbital and the Coulomb interaction between charges on atoms A and B, respectively. J^0_{AA}, which is equal to the difference between the ionization potential (IP) and the electron affinity (EA), is the second derivative of the energy with respect to the charge:

$$J^0_{AA} = \left(\frac{\partial^2 E}{\partial Q^2} \right)_{A_0} = \mathrm{IP} - \mathrm{EA}. \tag{5}$$

The condition $Q_{\mathrm{tot}} = \sum_{i=l}^{N} Q_i$ leads to a total of N coupled equations that must be solved for a given configuration. For large separations R between A and B, J_{AB} is given by

$$J_{AB}(R) = \frac{14.4}{R} \tag{6}$$

with R in angstroms and J_{AB} in eV. For short distances, the charge distributions of A and B overlap and a shielding correction must be applied [55]. This shielding correction is defined by considering the atomic density in terms of single Slater orbitals. For example, the normalized n_s Slater orbitals

are constructed as

$$\phi^{\text{slat}}_{n\zeta_i} = N_n r^{n-1} e^{\zeta_i r}, \tag{7}$$

where N_n is a normalization constant. The valence orbital exponent ζ_i (with i = A or B) is defined as

$$\zeta_i = \frac{\lambda(2n+1)}{2R_i}, \tag{8}$$

where R_i is the covalent radius in atomic units and λ an adjustable parameter to account for the difference between an average atom size and the covalent radius R_i. Similar equations are defined for all the outer valence orbitals such as the n_p and n_d orbitals. The EQeq method [56], which derives from the Qeq method, is based on a noniterative approach that fits the chemical potential to higher ionization energies. The improvement of this method compared to the Qeq method lies in the larger data set (i.e., larger number of ionization energies) used to calculate the electronegativity. The accuracy of this method was recently demonstrated for a set of Metal Organic Frameworks [56]. The Qeq charges were computed by using the Qeq code implemented in the GULP code [57], whereas the EQeq charges were computed by using the code published in Ref. [56].

(b) The *Mulliken and Löwdin charges* are obtained from the atomic orbitals projected on nonorthogonal and orthogonal basis sets, respectively [58,59]. The Mulliken population analysis distributes the electrons according to the atomic orbital occupancy [58]. Following the Mulliken formalism, the total *gross atomic population* G_A of an atom is equal to the sum of the *net atomic population* (electrons that belong to the orbitals centered on an atom) plus one half of the *overlap atomic population* (electrons shared between two atoms). The population matrix PM is built by using the density matrix P and the overlap matrix s for the ωth basis function in the λth orbital:

$$PM_{\omega\lambda} = (PS)_{\omega\lambda}. \tag{9}$$

The sum of all the $PM_{\omega\lambda}$ terms is defined as the *gross orbital product* G_0. The sum of G_0 over all the orbitals belonging to an atom is defined as the *gross atomic population* G_A. The Mulliken charge q of a given atom i is defined as the difference between the number of electrons of the isolated atom Z_i (which corresponds to the atomic number) and the *gross atomic population* G_A:

$$q_i = Z_i - G_A. \tag{10}$$

The Mulliken method ignores the differences between the chemical nature of the atoms involved (i.e., electronegativity), which can lead to nonphysical results such as negative orbital occupations for instance. Furthermore, it suffers from basis set dependency. The Löwdin population analysis was developed as an attempt to improve the description given by the Mulliken method. This method prevents the overoccupation of orbitals, which can occur in the Mulliken method. However, like the Mulliken method, the Löwdin method ignores the electronegativity of the different atoms which can lead to nonphysical charges. The Mulliken and Löwdin charges were computed using the CPMD code [60].

(c) The *ESP method* assigns point charges to the atomic centers in order to best reproduce the electrostatic potential on a fine grid surrounding the atoms [61]. The grid is chosen to lie outside of the van der Waals radius of each atom of the system. In highly packed solids, where there is little volume outside of the van der Waals radii of the atoms to define valid fitting points, ESP charges often fail to reproduce the electrostatic potential. The ESP charges were computed using the CPMD code [60].

(d) The *Bader method* assigns charges by partitioning the charge density grid into atomic volumes referred to as Bader volumes [62]. Typically, there is one charge density maximum at each atomic center and one Bader volume for each atom. The dividing surfaces separating these volumes, also called zero-flux surfaces, lie in the bonding regions between atoms. The Bader partitioning has the advantage over other partitioning schemes (e.g., Mulliken population analysis) that it is based on the charge density which is an *observable* [63]. Furthermore, in well converged electronic structure calculations, the charge density is insensitive to the basis set used. The Bader partitioning algorithm follows steepest ascent paths along the charge density gradient from a grid point to another until a charge density maximum is reached [64]. The Bader charges, which were computed using the code in Ref. [64], were obtained from the charge density obtained with the CPMD code [60].

III. STRUCTURAL PROPERTIES

A. Pair correlation functions

We first determined the structural properties of g-$GeS_2(s)$ by calculating the partial pair correlation functions $g_{\alpha\beta}(r)$ with α, β = Ge or S. In order to compare the partial pair correlation functions for g-$GeS_2(b)$ and g-$GeS_2(s)$, $g_{\alpha\beta}(r)$ for g-$GeS_2(s)$ have been corrected for the finite size of the sample [65–67]:

$$\tilde{g}_{\alpha\beta}(r) = \frac{g_{\alpha\beta}(r)}{f(r)} \text{ with } f(r) = 1 - \frac{r}{2h}, \tag{11}$$

where h is the thickness of the slab. While this correction is not needed to compare the position of the peaks in the $g_{\alpha\beta}(r)$ functions, it allows correcting the peak intensities for the finite size of the sample. The partial pair correlation functions $\tilde{g}_{GeS}(r)$, $\tilde{g}_{\text{GeGe}}(r)$, and $\tilde{g}_{SS}(r)$ for g-$GeS_2(s)$ are compared in Fig. 2 with those for g-$GeS_2(b)$. For each partial pair correlation function, we also show in Table I the position of the first peak, which indicates the nearest-neighbor distance. g-$GeS_2(b)$ and g-$GeS_2(s)$ show very similar Ge-S bond lengths (2.20 Å). These values are in agreement with the experimental Ge-S bond length for g-$GeS_2(b)$ (2.20–2.23 Å) [68,69]. Overall, the shape of the pair correlation functions for g-$GeS_2(b)$ and g-$GeS_2(s)$ are similar. The large amplitude of the first $g_{GeS}(r)$ peak for g-$GeS_2(b)$ and g-$GeS_2(s)$ indicates that heteropolar Ge-S bonding is the most common type of bonds in these systems. Differences are found in the amplitude of some of the peaks. For instance, the first peak in the g_{GeS}(r) function for g-$GeS_2(s)$ has a larger amplitude than its bulk counterpart. This difference is indicative of a larger content of Ge-S bonds with respect to the total numbers of bonds for g-$GeS_2(s)$.

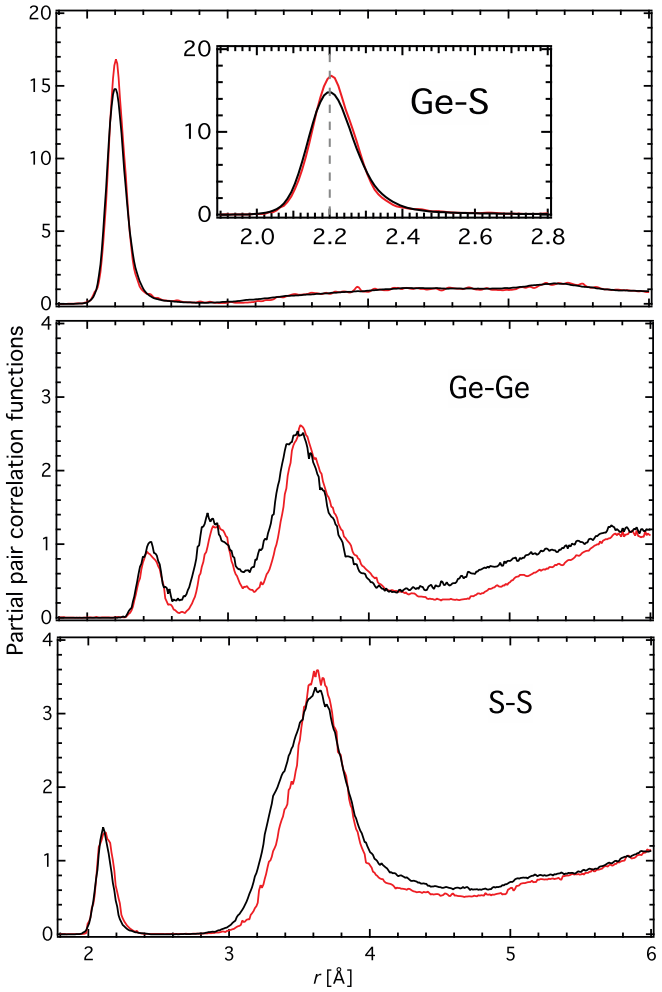

FIG. 2. (Color online) Ge-S (top), Ge-Ge (middle), and S-S (bottom) pair correlation functions: $g_{\alpha\beta}(r)$ for g-$GeS_2(b)$ (black line) and $\tilde{g}_{\alpha\beta}(r)$ for g-$GeS_2(s)$ (red line) at 300 K; the data for g-$GeS_2(s)$ were corrected for the finite size of the sample (see text). (Inset) Detailed view of the first peak for the $g_{GeS}(r)$. Dashed lines: position of the first peak of the Ge-S $g_{\alpha\beta}(r)$ for g-$GeS_2(b)$.

B. Atom coordination

The distributions of the coordination number (CN) around Ge and S atoms for the bulk and surface models are shown in Table II. For the surface models (i.e., at $T = 0$ K and $T = 300$ K) the CN distributions have been obtained by considering the top external layer within the last 10 Å. For both the bulk and surface models, CN is determined by computing the average number of atoms (Ge or S) within a cutoff distance from the S or Ge atoms. For each coordination type (Ge-Ge, Ge-S, and S-S), the cutoff distance was extracted from $g_{\alpha\beta}(r)$ in Fig. 2 as the position of the minimum between the first and the second peaks. We found 2.7 Å for Ge-Ge, 2.6 Å for S-S, and 2.9 Å for Ge-S. We highlight in Fig.1 the GeS_4 tetrahedra for the two surface models under consideration. g-$GeS_2(b)$ and g-$GeS_2(s)$ are mainly made of tetrahedrally coordinated Ge and twofold coordinated S. Although g-$GeS_2(s)$ is characterized by a relatively large free surface, the average CN of Ge and S are close to those of the bulk (Ge: 3.79 and S: 2.05). However, differences can be noted in the distribution of the individual coordinating units. When compared to the bulk counterpart, g-$GeS_2(s)$ shows a decrease in the numbers of fourfold (−3.6%, Ge_0S_4) and twofold (−2.5%) coordinated Ge, while there is an increase in the threefold coordination (+6.6%). Similarly, twofold coordinated S is decreased by 4.4%, which is mainly balanced by an increase of the threefold coordinated S atoms (+3.4%). These results show that g-$GeS_2(s)$ possesses a slightly lower chemical order than g-$GeS_2(b)$. As for the behavior of g-$GeS_2(s)$@0K, one notices a larger content of threefold coordinated S and three-coordinated Ge with respect to g-$GeS_2(s)$ at 300 K. We also determined the degree of homopolar bonding in g-$GeS_2(s)$. The fraction of homopolar bonding can be estimated as $f_{hp} = (n_{SS} + n_{GeGe})/n_{tot}$, where n_{SS} is the number of S-S bonds, n_{GeGe} is the number of Ge-Ge bonds, and n_{tot} is the total number of bonds. g-$GeS_2(s)$ and g-$GeS_2(b)$ feature similar fractions of homopolar bonds (∼16%).

TABLE I. Position in angstroms of the first peak in the partial $g_{\alpha\beta}(r)$ functions for g-$GeS_2(b)$ and g-GeS_2 surfaces [g-$GeS_2(s)$ and g-$GeS_2(s)$@0K]. We also report experimental values from the literature.

system	Ge-S	Ge-Ge	S-S
g-$GeS_2(b)$	2.20(2)	2.45(3)	2.11(3)
g-$GeS_2(s)$	2.20(3)	2.42(4)	2.12(3)
g-$GeS_2(s)$@0K	2.20(3)	2.42(4)	2.10(5)
Literature [68,69]	2.20-2.23	2.40(5)	2.10(2)

TABLE II. Percentage of l-coordinated Ge atoms for g-$GeS_2(b)$ and g-GeS_2 surfaces [g-$GeS_2(s)$ and g-$GeS_2(s)$@0K]. For four-coordinated Ge and two-coordinated S the contributions of S_4/Ge_1S_3 and $S_2/Ge_2/S_1Ge_1$ units are shown.

		g-$GeS_2(b)$	g-$GeS_2(s)$	g-$GeS_2(s)$@0K
Ge atom				
$l = 2$		6.0	3.6	0.81
$l = 3$		9.9	16.5	19.4
$l = 4$	S_4	70.5	66.9	66.1
	Ge_1S_3	11.6	11.5	12.1
$l = 5$		0.6	1.47	1.6
⟨CN⟩		3.79	3.78	3.81
S atom				
$l = 1$		0.8	1.7	1.2
$l = 2$	S_2	2.5	2.9	2.9
	Ge_2	73.9	69.5	69.6
	S_1Ge_1	17.7	17.2	17.1
$l = 3$		5.2	8.6	9.2
⟨CN⟩		2.05	2.07	2.08

C. Bond angle distributions

Figure 3 shows the S-Ge-S and Ge-S-Ge bond angles distributions (BAD) for g-$GeS_2(b)$ and g-$GeS_2(s)$. These

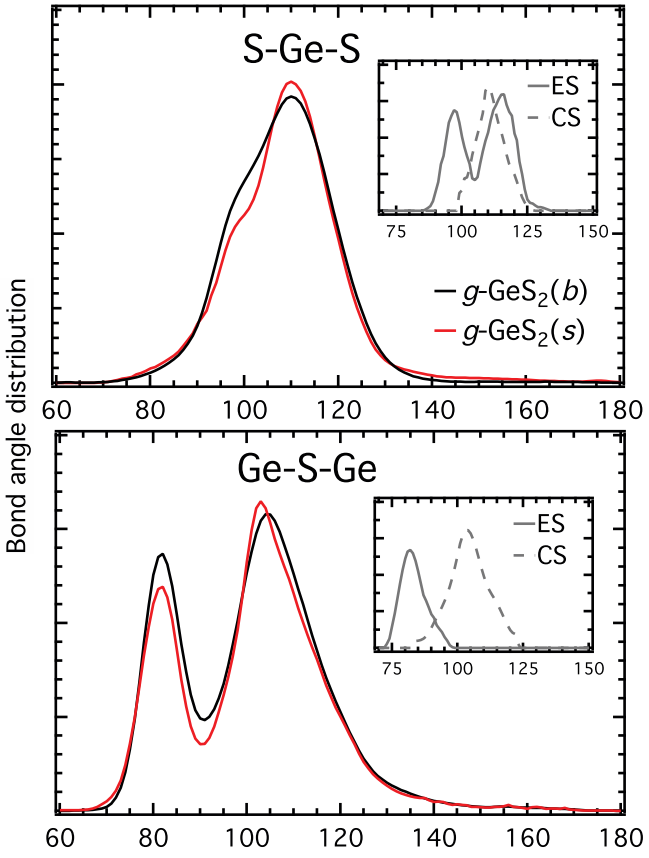

FIG. 3. (Color online) S-Ge-S (top) and Ge-S-Ge (bottom) bond-angle distributions (BAD). The black and red lines correspond to the data for g-$GeS_2(b)$ and g-$GeS_2(s)$, respectively. The inset shows the BAD for g-$GeS_2(s)$ which is decomposed in corner-sharing (CS, dashed line) and edge-sharing (ES, solid line) contributions.

distributions have been calculated by using the same cutoff distances as those used for the coordination numbers. The inset in Fig. 3 shows the contributions of corner-sharing and edge-sharing tetrahedra for g-$GeS_2(s)$ at 300 K. g-$GeS_2(b)$ and g-$GeS_2(s)$ show very similar BAD distributions, with only small differences in the amplitudes of the different contributions. The S-Ge-S BAD exhibits a broad peak at about 110° with a shoulder at 98°. These peaks correspond to angles in corner-sharing tetrahedra (109°) and angles in edge-sharing tetrahedra at 98° and 110°. The peak at 98° is due to the S-Ge-S angle involved between two Ge_1S_4 tetrahedra, which share an S-S edge. The peak at 110° is associated with S-Ge-S angles where one S is shared between two Ge_1S_4 tetrahedra and the other S is involved in a different structure unit. g-$GeS_2(s)$ shows a slightly larger peak at 110° and a slightly smaller peak at 98°. This result is indicative of a small increase in corner-sharing tetrahedra for g-$GeS_2(s)$ when compared to g-$GeS_2(b)$. The first peak at 83° in the Ge-S-Ge BAD arises from edge-sharing tetrahedra while the second peak at 103° is due to corner-sharing tetrahedra. g-$GeS_2(s)$ shows a larger peak at 103° and a lower peak at 83°. This result stems from the higher corner-sharing/edge-sharing ratio in g-$GeS_2(s)$ with respect to g-$GeS_2(b)$ and is consistent with the S-Ge-S BAD analysis above.

D. Structure factors

Total neutron structure factor $S_T(k)$ and the Faber-Ziman (FZ) partial structure factors were compared for g-$GeS_2(b)$ and g-$GeS_2(s)$ models:

$$S_T(k) - 1 = \sum_{\alpha=1}^{n}\sum_{\alpha=1}^{n} \frac{c_\alpha c_\beta b_\alpha b_\beta}{\langle b\rangle^2}\left[S^{FZ}_{\alpha\beta}(k) - 1\right], \qquad (12)$$

where α and β are the chemical species and $n = 2$ the number of different chemical species. c_α and b_α are the atomic fraction and coherent neutron scattering length of the chemical species α, $\langle b\rangle = c_{Ge}b_{Ge} + c_S b_S$ the coherent neutron-scattering length, and $S^{FZ}_{\alpha\beta}(k)$ the FZ partial structure. The coherent neutron-scattering lengths for Ge and S of natural isotopic abundance are $b_{Ge} = 8.185$ fm and $b_S = 2.847$ fm [70]. As shown in Fig. 4, the total structure factors $S_T(k)$ for g-$GeS_2(b)$ and g-$GeS_2(s)$ are very similar and show peaks at $k \sim 1$, ~2.1, and ~4 Å^{-1}. This is the mere consequence of close patterns for the FZ partial structure factors of g-$GeS_2(b)$ and g-$GeS_2(s)$ (Fig. 5). The peak at $k \sim 1$ Å^{-1} (known as first diffraction peak, FSDP) arises predominantly from the Ge-Ge correlations. The Ge-S correlations also contribute to the FSDP but to a much lower extent. The absence of any contribution at $k \sim 1$ Å^{-1} from the S-S correlations suggests that, for both g-$GeS_2(b)$ and g-$GeS_2(s)$ surface, Ge atoms account for most of the intermediate range structural order in amorphous GeS_2.

IV. ELECTRONIC PROPERTIES

A. Electronic density of states

The electronic properties of g-$GeS_2(s)$ were investigated by analyzing its electronic density of states (EDOS) (Fig. 6). The EDOS for g-$GeS_2(s)$ exhibits three bands: (A) [−16, −11 eV], (B) [−10, −6 eV] and (C) [−6, 0 eV]. The EDOS for g-$GeS_2(s)$ bears some resemblance with the experimental valence spectrum obtained for g-$GeS_2(b)$ [71]. The main difference between the EDOS for g-$GeS_2(b)$ and g-$GeS_2(s)$ concerns the pseudogap around the Fermi level. The EDOS around the Fermi level is deeper for g-$GeS_2(b)$.

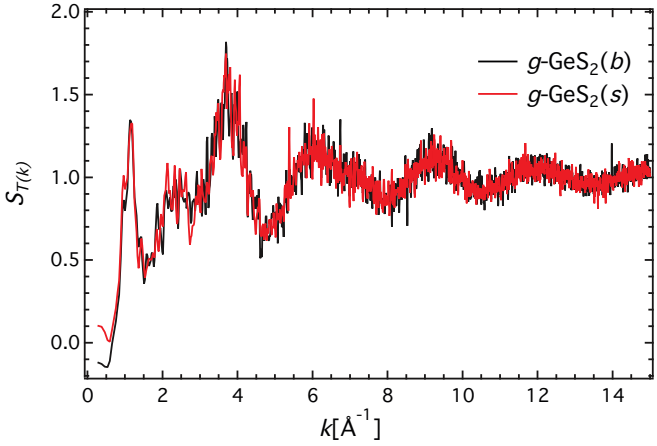

FIG. 4. (Color online) Total structure factors for g-$GeS_2(b)$ (black line) and the g-$GeS_2(s)$ model (red line).

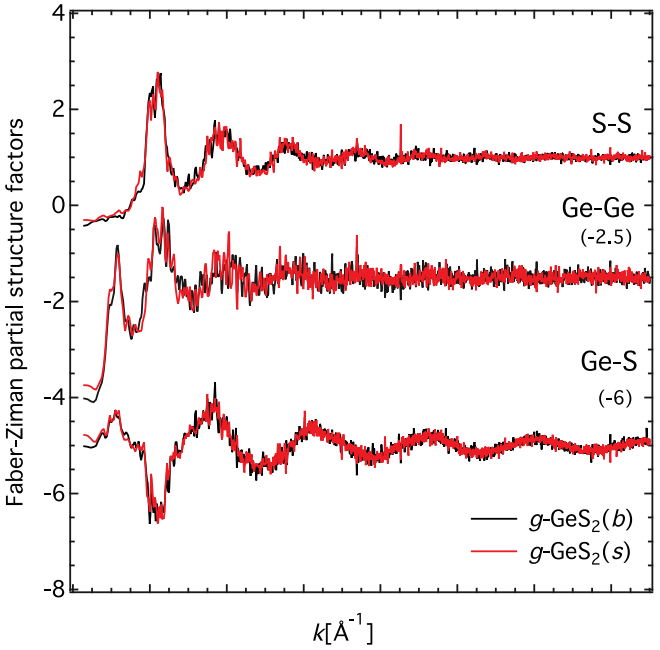

FIG. 5. (Color online) The Faber-Ziman partial structure factors $S^{FZ}_{SS}(k)$ (top), $S^{FZ}_{GeGe}(k)$ (middle), and $S^{FZ}_{GeS}(k)$ (bottom). The black and red lines correspond to the data for g-$GeS_2(b)$ and for g-$GeS_2(s)$, respectively.

B. Wannier functions

Figure 7 shows the positions of the centers of the Wannier functions (WF) in a molecular configuration of the surface model at $T = 300$ K. Fourfold coordinated Ge atoms are characterized by four WF centers resulting from the bonds established between Ge and its S neighboring atoms. For S, the existence of six valence electrons and the twofold coordination of S is at the origin of a specific pattern; two WF centers are localized close to the S atom, representing the two lone pairs of electrons not involved in chemical bonding. In what follows, these WF centers are referred to as WF_{lp} centers. The other two WF centers, which are localized along the S-X (with $X =$ Ge or S) bonds, reflect interatomic bonding. In what follows, they are referred to as WF_b centers. The Ge_1 atom in Fig. 7 is coordinated to four S atoms, with bond lengths equal to

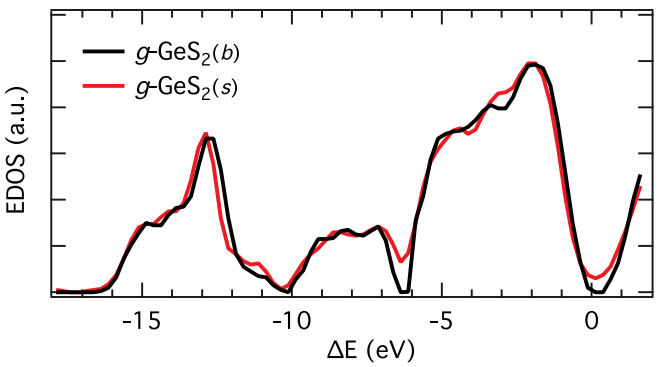

FIG. 6. (Color online) Electronic density of states (EDOS) extracted from the Kohn-Sham eigenvalues ($\Delta E = E - E_{Fermi}$) The black and red lines correspond to the data for g-$GeS_2(b)$ and for g-$GeS_2(s)$, respectively.

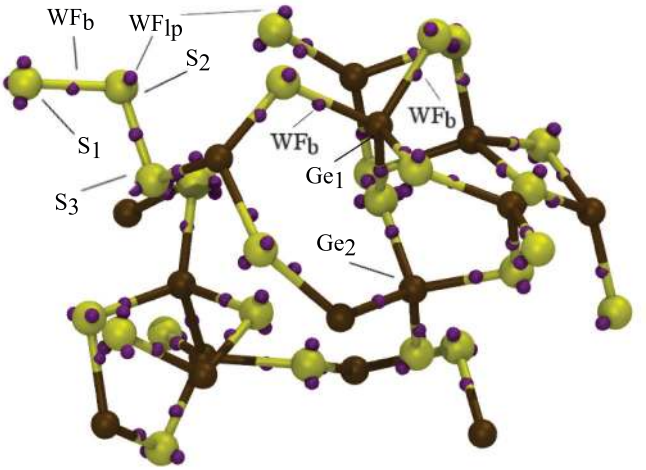

FIG. 7. (Color online) Zoom in a configuration of g-$GeS_2(s)$ showing both heteropolar and homopolar bonds. Details are given in the text. Ge and S atoms appear as ochre and yellow spheres, respectively. The purple spheres are the WF centers, which correspond to both lone (WF_{lp}) and bond pairs (WF_b) of electrons.

2.23 ± 0.02 Å. When the location of the WF center is taken with respect to half the bond distance, each WF center is found to be closer to the S atom than to the Ge_1 atom (S-WF distance: 0.89 ± 0.01 Å). This result illustrates the fact that Ge-S bonds are iono-covalent since a sizable electron transfer occurs towards the more electronegative atom (S). A different situation is encountered when examining the S_1-S_2 and S_2-S_3 homopolar bonds, whose lengths are equal to 2.07 ± 0.03 Å. In this case, there is a WF center for each S-S bond located in the middle of the bond, as expected due to the covalent character of S-S homopolar bonds.

Another example of WF centers for homopolar bonds is shown in Fig. 7 for the Ge_2 atom. This atom is involved in three Ge-S bonds and one homopolar bond (Ge-Ge). As expected, the Ge_2-Ge bond is characterized by a WF center located in the middle of Ge-Ge interatomic bond. In order to obtain a comprehensive picture of the location of the Wannier centers, Fig. 8 shows the pair correlation function $g_{SWF}(r)$

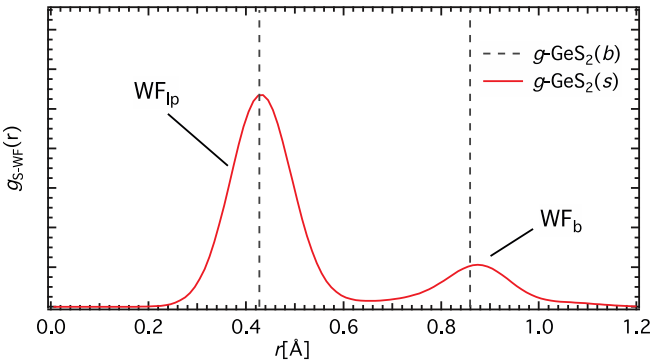

FIG. 8. (Color online) Correlation functions of S-WF pair, $g_{SWF}(r)$ for g-$GeS_2(s)$ (red line). The dashed lines show the position of the peaks for the g-$GeS_2(b)$. WF_{lp} and WF_b indicate the peaks due to the correlation between S atoms and the WF lone pairs and WF bonds, respectively (see text).

between the S atoms and the WF centers. $g_{SWF}(r)$ shows two peaks: a first peak centered at 0.435 Å and a second peak centered at 0.875 Å. The first peak corresponds to the distance between S atoms and the WF_{lp} centers. In contrast, the second peak corresponds to the distance between the S atoms and the WF_b centers. Such a S-WF_b distance, 0.875 Å, obtained for g-$GeS_2(s)$, is slightly larger than the value obtained for g-$GeS_2(b)$ (0.86 Å) [27] and lower than the value obtained for Se-WF_b (∼1 Å) in bulk g-$GeSe_2$ glass [26]. This result is consistent with the lower ionic character of the Ge-Se bond with respect to the Ge-S bond, and shows a slightly lower ionic character for g-$GeS_2(s)$ with respect to g-$GeS_2(b)$. The Ge-S bond shows a more pronounced ionic character compared to the Ge-Se bond, as discussed in Ref. [27] for g-$GeS_2(b)$. In contrast, the spreads of W_b and W_{lp} for g-$GeS_2(s)$ are slightly lower than those for g-$GeSe_2(b)$ ($W_b = 1.205 \pm 0.006$ Å and $W_{lp} = 1.21 \pm 0.01$ Å).

C. Atomic charges

Figure 9 shows the partial charges for Ge and S atoms as a function of the Ge and S atom coordinations. The results obtained for the different techniques are shown in Fig. 9. The Qeq and EQeq methods provide reasonable partial charges for both the Ge and S atoms as their absolute charge increases with the coordination. The Mulliken and Löwdin population lead to a nonzero net charge; this is due to the nontrivial problem

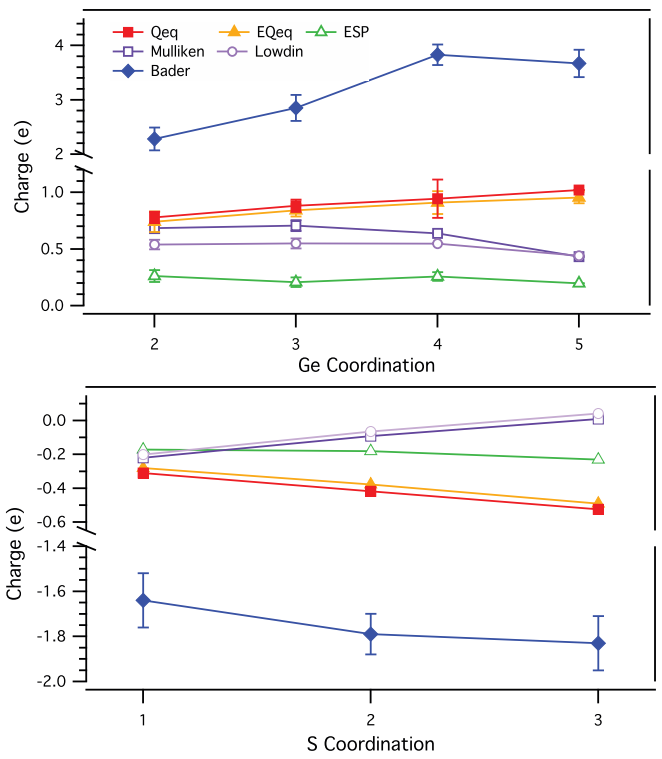

FIG. 9. (Color online) Ge (top) and S (bottom) partial atomic charges as a function of the coordination number, i.e., the total number of atoms (Ge or S) around a given atom. The different sets of data correspond to charges derived from the following methods: Qeq (red), EQeq (orange), Mulliken (purple), Löwdin (pink), ESP (green), and Bader (blue) (see text).

of projecting orbitals on a local basis with a non-negligible part of the electron density not assigned to a given atom. The ESP-derived charges are very low and nearly insensitive to the coordination number for both Ge and S atoms. This shows that the ESP-derived charges do not reflect the change in the bond chemistry as the local coordination around a Ge or S atom varies. The REPEAT method [72], which is a corrected version of the ESP method developed for periodic systems, was also tested but nonphysical partial charges were obtained for both Ge and S atoms; indeed we obtained negative charges for many Ge atoms and positive charges for many S atoms. The failure of the REPEAT method [72] for chalcogenide materials has been already reported [72]. This is due to the fact that the ESP methodology cannot reproduce the electrostatic potential for systems with high local atomic densities [72]. The Bader method leads to absolute charges which increase with the atomic coordination. The Voronoi method [64], which is similar to the Bader method with a different volumetric partitioning of the charge density, was also tested but very low charges and nearly insensitive to the coordination number were obtained for Ge and S atoms. The Qeq (EQeq) and Bader methods capture the effect of local coordination on the partial charges in chalcogenide materials. However, the absolute charges obtained by the Bader method are too large to be used, eventually, in potentials for classical simulations. Indeed, such large values, +3.83 for Ge^{IV} and −1.79 for S^{II}, would confer to the Ge and S atoms a nearly pure ionic character. For instance, these values are greater than most of the commonly used partial charges for silica. The charge-coordination correlation found in the Qeq method seems more appropriate to develop a force-field describing the interactions with a g-GeS_2 surface. Overcoordinated Ge (S) atoms possess a large positive (negative) charge with respect to that corresponding to stoichiometric coordination. This is directly related to their higher valence state which, in a formalism purely based on formal ionic charges [cations (Ge) and anions (S)], result in an increased charge localization. The Qeq approach seems to be the best suited technique to describe changes in the valence (charge) state for different coordinations. As far as this issue is concerned, the Qeq and EQeq methods produce a useful set of charges able to describe the structural order of g-GeS_2 materials.

V. CONCLUSION

The structural and electronic properties of amorphous chalcogenide GeS_2 surfaces make them promising candidates for applications in different domains. In particular, the high polarizability of chalcogenide surfaces (compared to most oxide-based materials) is of practical interest for heterogeneous catalysis and gas phase separation. Designing efficient processes using chalcogenide materials with high specific surface area (10–500 m^2/g) requires better understanding their surface properties. In this work, first-principles molecular dynamics was used to build a realistic model of g-GeS_2 surfaces. The properties of this surface model were then compared with those of bulk g-GeS_2. As in the case of bulk g-GeS_2, the g-GeS_2 surface model is mainly composed of fourfold coordinated Ge (Ge^{IV}) and twofold coordinated S (S^{II}). Despite a slightly different coordination distributions

(e.g., chemical disorder), the g-GeS_2 surface posseses a similar content of homopolar bonds with respect to bulk g-GeS_2. The electronic structure of g-GeS_2 was analyzed in terms of maximally localized Wannier centers. We found that the g-GeS_2 surface is characterized by a complex interplay between ionocovalent and covalent bonds similar to bulk g-GeS_2. However, the g-GeS_2 surface shows a slightly less ionic character than its bulk counterpart, but more ionic than g-$GeSe_2$.

Finally, different, yet complementary, charge-derivation methods were used to obtain the atomic partial charges for the g-GeS_2 surface. This charge estimate is important to construct a realistic interatomic potential in which the charges associated to each atomic site depends on its local coordination environment. The atomic charges found in this work will be employed to account for the electrostatic interactions in an empirical force field. The Qeq approach turns out to be the most suitable method for this purpose since it captures the change in the atomic partial charge upon changing the coordination of a given atom.

ACKNOWLEDGMENTS

This work was supported by the French Research Agency ANR within the framework of the project Nanochalco (ANR-11-BS08-015). This work was also supported by framework of the ICoME2 Labex (ANR-11-LABX-0053) and the A*MIDEX projects (ANR-11-IDEX-0001-02) cofunded by the French program "Investissements d'Avenir," which is managed by the ANR. We acknowledge the Centre Informatique National de l'Enseignement Supérieur (CINES) for a generous allocation on the supercomputer YODA (Project No. c2012096964). We thank T. K. Woo for providing us with the REPEAT method algorithm. We thank Massimo Celino (ENEA, Rome) for providing us a set of trajectories for glassy bulk GeS_2.

[1] A. Zakery and S. R. Elliott, in *Chalcogenide Glasses and their Applications in Optical Non-linearities* (Springer, Berlin, Heilderberg, New York, 2007).
[2] B. J. Eggleton, B. Luther-Davies, and K. Richardson, Nature Photon. **5**, 141 (2011).
[3] F. Jedema, Nature Mater. **6**, 90 (2007).
[4] M. Frumar, B. Frumarova, P. Nemec, T. Wagner, J. Jedelsky, and M. Hrdlicka, J. Non-Cryst. Solids **356**, 544 (2006).
[5] H. F. Hamann, M. O'Boyle, Y. C. Martin, M. Rooks, and H. K. Wickramasinghe, Nature Mater. **5**, 383 (2006).
[6] A. V. Kolobov, P. Fons, A. I. Frenkel, A. L. Ankudinov, J. Tominaga, and T. Uruga, Nature Mater. **3**, 703 (2004).
[7] R. K. Pan, H. Z. Tao, H. C. Zang, C. G. Lin, T. J. Zhang, and X. J. Zhao, J. Non-Cryst. Solids **357**, 2358 (2011).
[8] W.-S. Lim, S.-W. Kim, and H.-Y. Lee, J. Korean Phys. Soc. **51**, 1764 (2011).
[9] C. Lin, H. Tao, Z. Wang, B. Wang, H. Zang, X. Zheng, and X. Zhao, J. Non-Cryst. Solids **355**, 438 (2009).
[10] J. L. Mohanan, I. U. Arachchige, and S. L. Brock, Science **307**, 397 (2005).
[11] Y. Oh, C. D. Morris, and M. G. Kanatzidis, J. Am. Chem. Soc. **134**, 14604 (2012).
[12] S. L. Brock and H. Yu, in *Aerogels Handbook* (Springer, New York, Dordrecht, Heidelberg, London, 2011), p. 367.
[13] S. Bag, A. F. Gaudette, M. E. Bussell, and M. G. Kanatzidis, Nature Chem. **1**, 217 (2009).
[14] M. Shafaei-Fallah, A. Rothenberger, A. P. Katsoulidis, J. He, C. D. Malliakas, and M. G. Kanatzidis, Adv. Mater. **23**, 4857 (2011).
[15] G. S. Armatas and M. G. Kanatzidis, Nature Mater. **8**, 217 (2009).
[16] A. Hitihami-Mudiyanselage, K. Senevirathne, and S. L. Brock, ACS Nano **7**, 1163 (2013).
[17] B. J. Riley, J. Chun, J. V. Ryan, J. Matyas, X. S. Li, D. W. Matson, S. K. Sundaram, D. M. Strachan, and J. D. Vienna, RSC Adv. **1**, 1704 (2011).
[18] B. J. Riley, J. Chun, W. Um, W. C. Lepry, J. Matyas, M. J. Olszta, X. Li, K. Polychronopoulou, and M. G. Kanatzidis, Environ. Sci. Technol. **47**, 7540 (2013).
[19] C. Massobrio, M. Celino, P. S. Salmon, R. A. Martin, M. Micoulaut, and A. Pasquarello, Phys. Rev. B **79**, 174201 (2009).
[20] S. Le Roux, A. Bouzid, M. Boero, and C. Massobrio, Phys. Rev. B **86**, 224201 (2012).
[21] S. Le Roux, A. Zeidler, P. S. Salmon, M. Boero, M. Micoulaut, and C. Massobrio, Phys. Rev. B **84**, 134203 (2011).
[22] S. Le Roux, A. Bouzid, M. Boero, and C. Massobrio, J. Chem. Phys. **138**, 174505 (2013).
[23] M. Kibalchenko, J. R. Yates, C. Massobrio, and A. Pasquarello, Phys. Rev. B **82**, 020202 (2010).
[24] C. Massobrio, M. Micoulaut, and P. S. Salmon, Solid State Sci. **12**, 199 (2010).
[25] A. Bouzid and C. Massobrio, J. Chem. Phys. **137**, 046101 (2012).
[26] M. Bauchy, M. Micoulaut, M. Celino, S. Le Roux, M. Boero, and C. Massobrio, Phys. Rev. B **84**, 054201 (2011).
[27] M. Celino, S. Le Roux, G. Ori, B. Coasne, A. Bouzid, M. Boero, and C. Massobrio, Phys. Rev. B **88**, 174201 (2013).
[28] X. Zhang and D. A. Drabold, Phys. Rev. B **62**, 15695 (2000).
[29] F. Inam and D. A. Drabold, J. Non-Cryst. Solids **354**, 2495 (2008).
[30] J. Akola, J. Larrucea, and R. O. Jones, Phys. Rev. B **83**, 094113 (2011).
[31] R. Car and M. Parrinello, Phys. Rev. Lett. **55**, 2471 (1985).
[32] A. D. Becke, Phys. Rev. A **38**, 3098 (1988).
[33] C. Lee, W. Yang, and R. G. Parr, Phys. Rev. B **37**, 785 (1988).
[34] J. P. Perdew and Y. Wang, Phys. Rev. B **45**, 13244 (1992).
[35] M. Micoulaut, R. Vuilleumier, and C. Massobrio, Phys. Rev. B **79**, 214205 (2009).
[36] S. Grimme, J. Compt. Chem. **27**, 1787 (2006).
[37] K. E. Yousaf and E. N. Brothers, J. Chem. Theory Comput. **6**, 864 (2010).
[38] F. Shimojo, Z. Wu, A. Nakano, R. K. Kalia, and P. Vashishta, J. Chem. Phys. **132**, 094106 (2010).
[39] K. Koizumi, M. Boero, Y. Shigeta, and A. Oshiyama, J. Phys. Chem. Lett. **4**, 1592 (2013).
[40] M. Steinmetz and S. Grimme, ChemistryOpen **2**, 115 (2013).
[41] N. Troullier and J. L. Martins, Phys. Rev. B **43**, 1993 (1991).

[42] S. Nosé, Mol. Phys. **52**, 255 (1984).
[43] S. Nosé, J. Chem. Phys. **81**, 511 (1984).
[44] W. G. Hoover, Phys. Rev. A **31**, 1695 (1985).
[45] G. J. Martyna, M. L. Klein, and M. Tuckerman, J. Chem. Phys. **97**, 2635 (1992).
[46] R. Resta and S. Sorella, Phys. Rev. Lett. **82**, 370 (1999).
[47] N. Marzari and D. Vanderbilt, Phys. Rev. B **56**, 12847 (1997).
[48] N. Marzari, A. A. Mostofi, J. R. Yates, I. Souza, and D. Vanderbit, Rev. Mod. Phys. **84**, 1419 (2012).
[49] G. H. Wannier, Phys. Rev. **52**, 191 (1937).
[50] M. Sharma, Y. Wu, and R. Car, Int. J. Quantum Chem. **95**, 821 (2003).
[51] R. Scipioni, D. A. Schmidt, and M. Boero, J. Chem. Phys. **130**, 024502 (2009).
[52] M. Boero, M. Parrinello, S. Huffer, and H. Weiss, J. Am. Chem. Soc. **122**, 501 (2000).
[53] P. L. Silvestrelli, N. Marzari, D. Vanderbit, and M. Parrinello, Solid State Commun. **107**, 7 (1998).
[54] S. V. Sukhomlinov and K. S. Smirnov, J. Phys. Condens. Matter. **24**, 475501 (2012).
[55] A. K. Rappe and W. A. Goddard III, J. Phys. Chem. **95**, 3358 (1991).
[56] C. E. Wilmer, K. C. Kim, and R. Q. Snurr, J. Phys. Chem. Lett. **3**, 2506 (2012).
[57] J. D. Gale and A. L. Rohl, Mol. Simul. **29**, 291 (2003).
[58] R. S. Mulliken, J. Chem. Phys. **23**, 1833 (1955).
[59] P.-O. Löwdin, J. Chem. Phys. **18**, 365 (1950).
[60] CDMP, http://www.cpmd.org/, Copyright IBM Corp 1990-2008, Copyright MPI für Festkörperforschung Stuttgart 1997-2001.
[61] S. R. Cox and D. E. Williams, J. Comput. Chem. **2**, 304 (1981).
[62] R. F. W. Bader, *Atoms in Molecules: a Quantum Theory* (Oxford University Press, New York, 1990).
[63] C. Gatti and P. Macchi, in *Modern Charge-Density Analysis* (Springer, Dordrecht, Heidelberg, London, New York, 2012).
[64] W. Tang, E. Sanville, and G. Henkelman, J. Phys.: Condens. Matter, **21**, 084204 (2009).
[65] B. Siboulet, B. Coasne, J.-F. Dufrêche, and P. Turq, J. Phys. Chem. B **115**, 7881 (2011).
[66] M. Lei, A. M. R. de Graff, M. F. Thorpe, S. A. Wells, and A. Sartbaeva, Phys. Rev. B **80**, 024118 (2009).
[67] B. Coasne and J. T. Fourkas, J. Phys. Chem. C **115**, 15471 (2011).
[68] A. Ziedler, W. E. Drewitt, P. S. Salmon, A. C. Barnes, W. A. Crichton, S. Klotz, H. E. Fischer, C. J. Benmore, S. Ramos, and A. C. Hannon, J. Phys.: Cond. Mat. **21**, 474217 (2009).
[69] A. Bytchkov, G. J. Cuello, S. Kohara, C. J. Benmore, D. L. Price, and E. Bychkova, Phys. Chem. Chem. Phys. **15**, 8487 (2013).
[70] I. Petri and P. S. Salmon, J. Non-Cryst. Solids **293–295**, 169 (2001).
[71] D. Foix, H. Martinez, A. Pradel, M. Ribes, and D. Gonbeau, Chem. Phys. **323**, 606 (2006).
[72] C. Campañá, B. Mussard, and T. K. Woo, J. Chem. Theory Comput. **5**, 2866 (2009).